

Available online at [www.sciencedirect.com](http://www.sciencedirect.com)2014, 26(5):780-795  
DOI: 10.1016/S1001-6058(14)60087-1[www.sciencedirect.com/  
science/journal/10016058](http://www.sciencedirect.com/science/journal/10016058)

## Marine propellers performance and flow-field prediction by a free-wake panel method\*

GRECO Luca, MUSCARI Roberto, TESTA Claudio  
 CNR-INSEAN, Italian Ship Model Basin, Rome, Italy, E-mail: luca.greco@cnr.it  
 DI MASCIO Andrea  
 CNR-IAC, Istituto per le Applicazioni del Calcolo “M. Picone”, Rome, Italy

(Received August 6, 2013, Revised April 30, 2014)

**Abstract:** A Boundary Element Method (BEM) hydrodynamics combined with a flow-alignment technique to evaluate blades shed vorticity is presented and applied to a marine propeller in open water. Potentialities and drawbacks of this approach in capturing propeller performance, slipstream velocities, blade pressure distribution and pressure disturbance in the flow-field are highlighted by comparisons with available experiments and RANSE results. In particular, correlations between the shape of the convected vortex-sheet and the accuracy of BEM results are discussed throughout the paper. To this aim, the analysis of propeller thrust and torque is the starting point towards a detailed discussion on the capability of a 3-D free-wake BEM hydrodynamic approach to describe the local features of the flow-field behind the propeller disk, in view of applications to propulsive configurations where the shed wake plays a dominant role.

**Key words:** BEM hydrodynamics, free-wake analysis, BEM-RANSE comparison

### Introduction

A hydrodynamic formulation based on a Boundary Element Method (BEM) is herein presented and applied to marine propellers in open water conditions. Aim of the work is to investigate the capabilities of a 3-D free-wake panel method in predicting the behaviour of propellers in terms of delivered thrust and torque, velocity field downstream the propeller disk, blade pressure loads and flow-field radiated noise. In the framework of potential flows, it is well known that propeller hydroloads strongly depend on the vorticity field released from the blade trailing edge (potential wake), especially for low-speed conditions, where the vortex-sheet is closer to the propeller plane. In the past there has been a growing research interest in correlating both wake pitch and tip-vortex roll up with propeller operating conditions, early relevant investigations, carried out by potential flow methods, are due to Kerwin and Lee<sup>[1]</sup>, whereas semi-empirical procedures to tailor wake pitch and contraction to flow con-

ditions and propeller loading are discussed, for instance, in Hoshino<sup>[2]</sup>. In the attempt of detecting the wake shape as solution of the potential flow hydrodynamics, Greely and Kerwin<sup>[3]</sup> and later Kinnas and Pyo<sup>[4]</sup> proposed a devoted vortex lattice method whilst Liu and Colbourne<sup>[5]</sup> suggested a BEM approach coupled with a suitable wake surface relaxation scheme. More recently BEM hydrodynamics combined with efficient wake alignment procedures have been presented to study marine propellers in open water and unsteady conditions due to manoeuvres or hull wake onset flow<sup>[6-8]</sup>. These works well highlight the capability of a free-wake BEM solver to predict propeller performance in terms of blade pressure distribution and thrust/torque. However, very few attempts of verifying flow-field velocity features, pressure signals behind the propeller disk or wake shape exist; an example is provided in Liu and Colbourne<sup>[5]</sup>, where comparisons between numerical results and available experiments are shown only in terms of azimuthally-averaged velocity fields. Although satisfactory BEM propeller performance predictions may be obtained through rough vortex-sheet modelling (especially close to the design condition, where the rigid-wake approach is widely used), the study of many problems of practical interest

\* **Biography:** GRECO Luca (1976-), Male, Ph. D., Researcher

needs accurate wake shape predictions to yield a detailed description of the induced velocity perturbations. This is particularly true when simplified hydrodynamic propeller models, based on airfoil theories corrected with the induced-velocity field due to propeller wake, are used as fast and reliable solvers in preliminary/optimal design process<sup>[9]</sup>, as well as in the hydro-acoustic analysis of propellers through the Bernoulli theorem<sup>[10]</sup> or in the study of unsteady hydrodynamic loads due to body-wake interaction<sup>[11]</sup>.

In view of the above considerations, this work presents a comprehensive assessment of a fully 3-D free-wake BEM formulation for marine propeller hydrodynamics. A *zero-th* order BEM is here combined with a devoted wake alignment procedure to detect the potential wake evolution, whereas the Bernoulli theorem is used for propeller hydroacoustics. The analysis of flow-field quantities like downstream vorticity (i.e., wake shape), velocity and pressure disturbances is investigated in details. The proposed BEM methodology has been developed during the past years and applied to study marine propellers cavitation<sup>[12]</sup> and hydro-acoustics<sup>[13]</sup>. For a four-bladed propeller in open water, validation results are herein provided through comparisons with experimental data including propeller open water curves and wake-field flow measurements by particle image velocimetry (PIV) technique. In addition, computations provided by an extensively validated RANSE solver<sup>[14,15]</sup> are used as reference results.

The proposed formulation is not a novelty in the context of potential flow hydrodynamics. However, in authors' opinion, such a thorough validation study, covering global and local propeller flow aspects, as well as experimental and computational reference data, may provide a useful guideline on the effectiveness and robustness of free-wake BEM-based approaches to face the analysis of marine configurations like propeller-rudder, pulling pods and contra-rotating propellers, where the propeller-induced wake plays a crucial role.

## 1. Theoretical models

### 1.1 3-D free-wake Boundary Element Method

A BEM for the analysis of inviscid flows around propellers in uniform flow is herein outlined. Details, summarized in Appendix A, are reported in Greco et al.<sup>[16]</sup>. Under the assumption of incompressible, inviscid and irrotational flow, the perturbation velocity potential field is governed by the Laplace equation  $\nabla^2 \varphi = 0$  that may be solved through the following Boundary Integral Representation (BIR) everywhere in the field<sup>[17]</sup>

$$E(\mathbf{x})\varphi(\mathbf{x}) = \oint_{S_B} \left( \frac{\partial \varphi}{\partial n} G - \varphi \frac{\partial G}{\partial n} \right) dS(\mathbf{y}) - \int_{S_w} \Delta\varphi \frac{\partial G}{\partial n} dS(\mathbf{y}) \quad (1)$$

with  $\mathbf{x}$  denoting a field point,  $S_B$  the propeller surface,  $S_w$  the convected wake,  $\mathbf{n}$  the local unit normal and  $\mathbf{y}$  a point on the boundary surfaces. In the framework of potential flows, the wake represents a zero-thickness layer departing from the trailing edge of lifting bodies where generated vorticity is shed downstream. Symbol  $\Delta\varphi$  indicates the potential jump across  $S_w$ , whereas  $G$  and  $\partial G / \partial n$  are the unit source and dipole in the unbounded 3-D space, respectively. Finally,  $E(\mathbf{x})$  is a domain function defined as 1, 1/2 or 0 for  $\mathbf{x}$  inside the flow-field, on the solid boundary surface or inside the solid body, respectively. Enforcement of Eq.(1) on the propeller surface yields a Boundary Integral Equation (BIE) for the velocity potential where unknowns are distributed over the propeller surface ( $\varphi$ ) and wake ( $\Delta\varphi$ ). Impermeability condition on  $S_B$  and the Kutta-Morino condition<sup>[17]</sup> on  $S_w$  are introduced for the wellposedness of the problem. For blunt trailing edges and strong 3-D flows (such as the case of highly loaded propellers), the Kutta-Morino condition fails and the use of an iterative algorithm is needed to assure a zero pressure jump (see Appendix A).

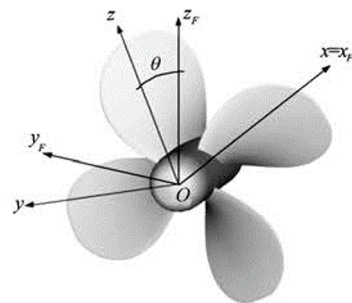


Fig.1 INSEAN E779A model propeller: 3-D view and definition of fixed frame of reference (FFR) and rotating frame of reference (RFR) at time  $t > 0$  (right-handed screw)

After discretization of  $S_B$  and  $S_w$  into surface panels and enforcement of Eq.(1) at the centroids of the body panels, the application of a *zero-th* order BEM yields a linear set of algebraic equations in terms of  $\varphi$  on the body surface. The pressure field upon the blade(s) is then computed by the Bernoulli equation that, written in the rotating frame of reference fixed to propeller blades (see Fig.1), reads

$$\frac{1}{2}q^2 + \frac{p}{\rho} + gz_0 = \frac{1}{2}v_i^2 + \frac{p_0}{\rho} \quad (2)$$

where  $p_0$  represents the free-stream reference pressure,  $\rho$  the water density,  $gz_0$  the hydrostatic head term referred to a reference vertical position (i.e., the waterline),  $v_i = v_0 + \omega \times x$  the inflow velocity at point  $x$  (being  $v_0$  the advancing speed and  $\omega$  the propeller angular velocity) and  $q = \|v_i + \nabla \phi\|$  the relative flow velocity. By integrating normal and tangential stress over blades surfaces, propeller forces and moments are obtained. A rough estimation of the viscosity-induced tangential stresses is here used: under the simplified assumption that the boundary-layer on the blade surface behaves like that over a flat plate at Reynolds number matching propeller operating conditions, tangential stresses are obtained from the Blasius theory<sup>[18]</sup> and the Grigson formula<sup>[19]</sup> for laminar and turbulent flows, respectively.

The numerical solution of the integral Eq.(1) requires the knowledge of the wake shape  $S_w$  that, in turn, depends on the loads delivered by propeller blades. Hence,  $S_w$  is not known *a priori* but it is part of the flow-field solution. A simple (linear) approach assumes the wake as a helicoidal surface with a pitch distribution accounting for the advancing speed and induced velocity from the Momentum Theory<sup>[20]</sup>. This rigid wake model allows to capture the global effect of trailing vorticity on propeller loads: however, a more physically consistent wake shape is needed when details of the flow-field downstream the propeller have to be investigated. A flow aligned wake may be determined by a nonlinear procedure where wake grid points are aligned to the local flow-field and the velocity perturbation is computed through a BIR derived by the gradient of Eq.(1). Specifically, the alignment technique used in this work consists of the following four steps: (1) initial guess for  $S_w$  based on a rigid wake assumption to estimate  $\phi$  on  $S_B$ , (2) evaluation of  $\nabla \phi$  on wake grid points (3) wake shape update through the following (pseudo) lagrangian scheme

$$x_w(t + \Delta t) = x_w(t) + \int_t^{t + \Delta t} [\nabla \phi(x_w, \hat{t}) + v_i] dt \quad (3)$$

where wake grid points are moved parallel to the local velocity field during the pseudo-time step  $\Delta t$ , (4) BIE solution update (see Eq.(1)) and further  $\nabla \phi$  computation on the updated  $S_w$  shape. The procedure is iterated up to convergence. The velocity field on the wake is evaluated by taking the gradient of Eq.(1) enforced

on wake grid points

$$\begin{aligned} \nabla_x \phi(x_w) &= \oint_{S_B} \left[ \frac{\partial \phi}{\partial n} \nabla_x G - \phi \nabla_x \left( \frac{\partial G}{\partial n} \right) \right] dS(y) \\ &\quad - \int_{S_w} \Delta \phi \nabla_x \left( \frac{\partial G}{\partial n} \right) dS(y) \end{aligned} \quad (4)$$

where symbol  $\nabla_x$  denotes the gradient operator acting on  $x_w$ . The wake induced-velocity at  $x_w$  is carried out invoking the vortex-doublet equivalence and using the Biot-Savart law applied to the vortices having the shape of the wake panel edges and intensity  $\Delta \phi$ . To assure a stable and regular numerical solution, a finite-thickness vortex model yielding a finite distribution of velocity within the vortex core is introduced, according to Suci and Morino<sup>[21]</sup>

$$v_n = \frac{1}{4\pi} \int_{\Gamma} \frac{r \times dy}{r^3}, \quad r \geq r_c \quad (5a)$$

$$v_n = \frac{v_{nc} r}{r_c}, \quad r < r_c \quad (5b)$$

where  $v_n$  denotes the velocity induced by a vortex line  $\Gamma$ ,  $r_c$  is the vortex core radius and  $r = x_w - y$ . Inside the vortex core,  $v_{nc}$  is evaluated by the Biot-Savart law for  $r = r_c$ . Wake alignment stability is enhanced by imposing  $r_c = r_{c0} \sqrt{1 + \Delta r_c \xi}$  with  $r_{c0}$  representing the vortex core radius at the blade trailing edge,  $\xi$  the arc length in the streamwise direction and  $\Delta r_c$  a suitable growth factor. The role played by both vortex core and blade-wake discretization, in terms of consistency and stability of the numerical scheme, is discussed in Greco et al.<sup>[16]</sup> where guidelines on the choice of  $r_{c0}$  and  $\Delta r_c$  are provided.

## 1.2 RANSE viscous flow model

The viscous flow solver<sup>[15,22]</sup> is based on the integration of the Reynolds averaged Navier-Stokes equations written in the rotating frame of reference (see Fig.1) in terms of absolute velocity components. These equations, cast in non-dimensional form by using a reference length  $L_{ref}$ , velocity  $U_{ref}$  and density  $\rho_{ref}$ , read

$$\begin{cases} \nabla \cdot u = 0 \\ (u - \omega \times r) \cdot \nabla u + \omega \times u + \nabla p - \nabla \cdot \tau = 0 \end{cases} \quad (6)$$

**Table 1** INSEAN E779A model propeller: geometry details

Propeller diameter	Number of blades	Pitch ratio (nominal)	Rake (nominal)	Expanded area ratio	Hub diameter (at prop. ref. line)
$D = 0.22727 \text{ m}$	$Z = 4$	$P/D = 1.1$	$i = 4^\circ 35'$	EAR = 0.689	$D_H = 0.04553 \text{ m}$

where  $\mathbf{u}$  denotes the absolute velocity,  $\mathbf{r} = \mathbf{x} - \mathbf{x}^0$  the position of point  $\mathbf{x}$  with respect to the origin of the fixed frame of reference  $\mathbf{x}^0$ ,  $\boldsymbol{\tau} = \nu_T (\nabla \mathbf{u} + \nabla \mathbf{u}^\top)$  the stress tensor,  $\nu_T = 1/Re + \nu_t$ ,  $\nu_t$  being the turbulent viscosity calculated by a proper turbulence model,  $Re$  the Reynolds number ( $Re = U_{ref} L_{ref} / \nu$ ) and  $\nu$  the physical kinematic viscosity of the fluid. Suitable boundary conditions are enforced at the physical boundaries of the numerical domain. Specifically, on the solid walls fluid velocity is set equal to the local velocity of the body at the inflow, the velocity is set to the undisturbed flow value whereas at the outflow the velocity is extrapolated from inner points. The numerical algorithm is based on a finite volume technique with pressure and velocity co-located at cell center. Viscous terms are integrated by a standard second order centered scheme, whereas for the convective and pressure terms a third order upwind scheme is used. Due to the treatment of viscous terms, the scheme remains formally second order in space. A chimera algorithm is implemented to use a mesh composed by structured, partially overlapping blocks. A divergence free velocity field is obtained by introducing a pseudo-time derivative in the discrete system of equations<sup>[23]</sup>. The convergence ratio in the pseudo-time is enhanced through local pseudo-time stepping, an implicit Euler scheme with approximate factorization<sup>[24]</sup> and a multi-grid technique<sup>[25]</sup>. Finally, in all the simulations shown in the following, the one-equation model by Spalart and Allmaras is used to compute  $\nu_t$ .

## 2. Numerical results

The proposed 3-D free-wake BEM approach is hereafter applied for the analysis of marine propeller performance and induced flow-field features in open water. By virtue of extensive CFD and experimental studies carried out at INSEAN in the past, the INSEAN E779A right-handed model propeller is considered<sup>[26]</sup>. A 3-D view of the propeller model is depicted in Fig.1 whereas basic geometry details are summarized in Table 1.

BEM computations are performed with discretization settings ensuring negligible sensitivity to further refinements. For conciseness, the convergence analysis is not shown here: as a final result, 48 chordwise and spanwise panels discretize propeller blades

surfaces whilst  $N_r = 180$  panels per turn discretize the wake sheet, composed of three wake turns. The free-wake analysis is performed using a pseudo-time step  $\Delta t = 1/N_r$  whereas the nondimensional vortex core radius and growth factor are chosen in relation to the advance coefficient, in particular,  $r_{\varepsilon 0} = 2.0 \times 10^{-2}$  and  $\Delta r_\varepsilon = 5.0$  for  $J \geq 0.88$  and  $r_{\varepsilon 0} = 3.0 \times 10^{-2}$  and  $\Delta r_\varepsilon = 20.0$  for  $J < 0.88$  are used. The iterative procedure stops when the root-mean-square of wake grid points displacements between two subsequent iteration steps is less than  $10^{-5}$ . More information about the behaviour of the free-wake algorithm in the solution seeking process is found in Greco et al.<sup>[16]</sup>.

RANSE simulations (used as reference results throughout the paper) are performed on two grid levels, the coarse grid stemming from the fine one by removing every other point. Uncertainty analysis, performed according to Roache<sup>[27]</sup>, shows a numerical uncertainty on propeller loads prediction of less than 1.5% and 4.9% for the delivered thrust and torque, respectively. RANSE computations shown in the following are obtained on the fine grid.

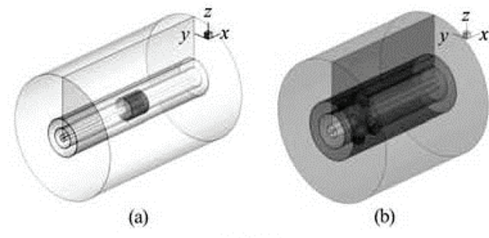


Fig.2 RANSE grid topology: overview (left) and near field (right)

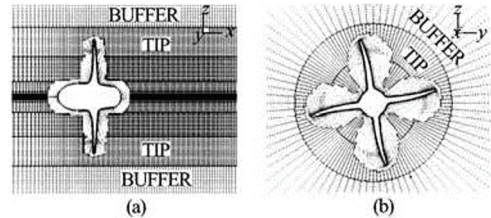


Fig.3 Details of the volume mesh for the RANSE solver. Section  $y_F/R = 0$  (left) and  $x_F/R = 0$  (right)

Figure 2 shows the building blocks of the mesh: the one around each blade and the hub is built with an

“O-topology” whereas toroidal blocks cover the whole background. An idea on the cell clustering is given in Fig.3, where two slices in the planes  $y_F/R = 0$  and  $x_F/R = 0$  are depicted. Note that a suitable fine grid is used to discretize the computational domain up to 4.4 radii downstream the propeller disk, within this region the RANSE solver is expected to properly capture the main flow features, like tip and hub vortices. Outside (see the buffer zone in Fig.3) a coarser mesh is used. The far field, where the inflow and outflow boundary conditions are enforced, is described by an even coarser mesh that extends about 23 radii upstream, 23 radii downstream and 16 radii in the radial direction. About 32 cells are put within the boundary layer thickness, the first point being located at a distance from the wall such that  $y^+ < 1$  in wall units. The different blocks sum up to a total of 11M cells.

## 2.1 Propeller performance

In this section BEM and RANSE hydrodynamic models are applied to predict propeller thrust  $T$  and torque  $Q$ . The following definitions of nondimensional force and moment coefficients are used:  $K_T = T / \rho n^2 D^4$ ,  $K_Q = Q / \rho n^2 D^5$ , where  $n$  denotes the rotational speed. As previously stated, the wake shape plays a crucial role in the framework of potential flows. In this context, Fig.4 shows a comparison between propeller performance coming from the free-wake ( $f_w$ ) and prescribed-wake ( $p_w$ ) BEM approach. Note that the prescribed wake pitch is here set using the experimental open water propeller thrust data as input of the Momentum Theory.

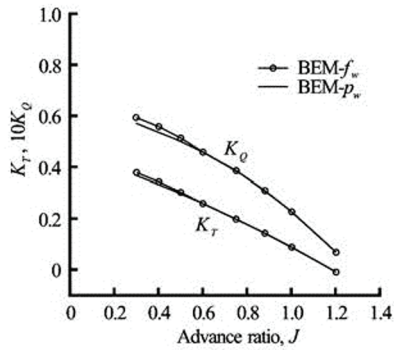


Fig.4 Performance results by BEM: prescribed wake ( $p_w$ ) and free-wake ( $f_w$ ) predictions compared

As shown, such *ad hoc* prescribed wake model is fully adequate to capture the effects induced by the vortex-sheet on propeller hydrodynamic loads, for advance ratios  $J = v_0/nD$  greater than 0.5. Differently, at  $J < 0.5$ , this modeling yields slightly under-

estimated loads, especially in terms of torque. Unless differently specified, the following BEM computations refer to the free-wake algorithm combined with the Iterative Pressure Kutta (IPK) technique to enforce  $\Delta p = 0$  at blade blunt trailing edge (see Appendix A). Comparisons between BEM predictions (with and without the IPK algorithm) and available experiments are depicted in Fig.5, as shown, better agreement is achieved by BEM-IPK algorithm, especially for  $J < 0.88$  (design value). At  $J > 0.88$ , 3D-flow effects decrease and, in turn, the application of the iterative Kutta condition is not needed. As it shall be clear in the following, increasing discrepancies at  $J < 0.6$  are mainly due to the formation of a leading edge vortex in the outer sections of the blade not modeled by the present BEM formulation, where the detachment of the trailing vortex is enforced at the blade tip.

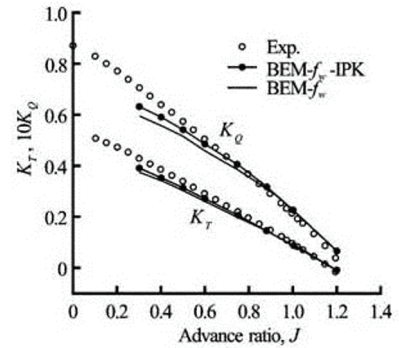


Fig.5 Free-wake BEM results (with and w/o IPK condition) compared to experiments

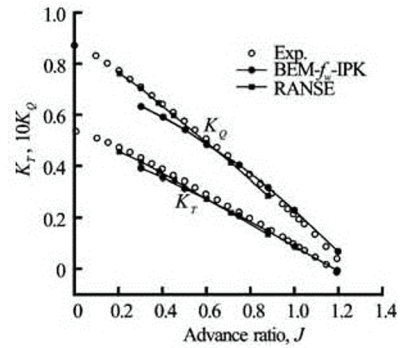


Fig.6 Performance results by BEM compared to experiments and RANSE computations

Figure 6 compares BEM-IPK outcomes with those computed by the RANSE solver and experiments. As expected, RANSE solver behaves better than the BEM-IPK at  $J < 0.6$ , whilst for  $J > 0.6$  both approaches exhibit a good agreement with experiments. For the sake of completeness, Table 2 summarizes BEM, RANSE and experimental outcomes, at three advance ratios, namely 0.3, 0.6, and 0.88.

**Table 2** BEM and RANSE thrust and torque predictions compared to experimental data

$J$	$K_T^{\text{BEM}}$	$K_T^{\text{RANSE}}$	$K_T^{\text{EXP}}$	$K_Q^{\text{BEM}}$	$K_Q^{\text{RANSE}}$	$K_Q^{\text{EXP}}$
0.30	0.391	0.416	0.430	0.0632	0.0701	0.0707
0.60	0.269	0.272	0.292	0.0483	0.0490	0.0506
0.88	0.147	0.133	0.157	0.0318	0.0286	0.0305

## 2.2 Propeller flow-field features

Predictions of the flow-field downstream the propeller disk are presented in this section. Nondimensional velocities respect to  $nD$  are shown. In the Fixed Frame of Reference (FFR) shown in Fig.1, axial and radial velocities,  $V_x$  and  $V_r$ , are positive along the  $x_F$  axis and outward, respectively, whereas the tangential velocity  $V_t$  is positive clockwise, as seen from downstream.

The design condition ( $J = 0.88$ ) is first analyzed. The capability of a rigid-wake modelling in detecting flow-field features downstream the propeller disk is discussed by comparing results from the free-wake approach and the *ad hoc* prescribed wake type.

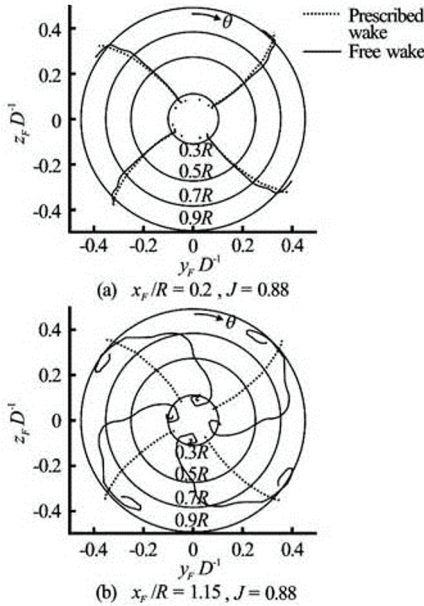


Fig.7 BEM prescribed and free-wake locations on transversal planes at  $x_F/R = 0.2$  (top) and  $x_F/R = 1.15$  (bottom),  $J = 0.88$

Outcomes, depicted in Fig.7, in terms of wake locations on transversal planes at  $x_F/R = 0.2$  (top) and  $x_F/R = 1.15$  (bottom), highlight the inadequacy of prescribed wake modelling, because, except close to the propeller disk, wake angular positions and overall shape do not match those predicted by the free-wake solution. In addition, surface roll-up near the blade tip is completely missed. These discrepancies strongly affect the prediction of the downstream

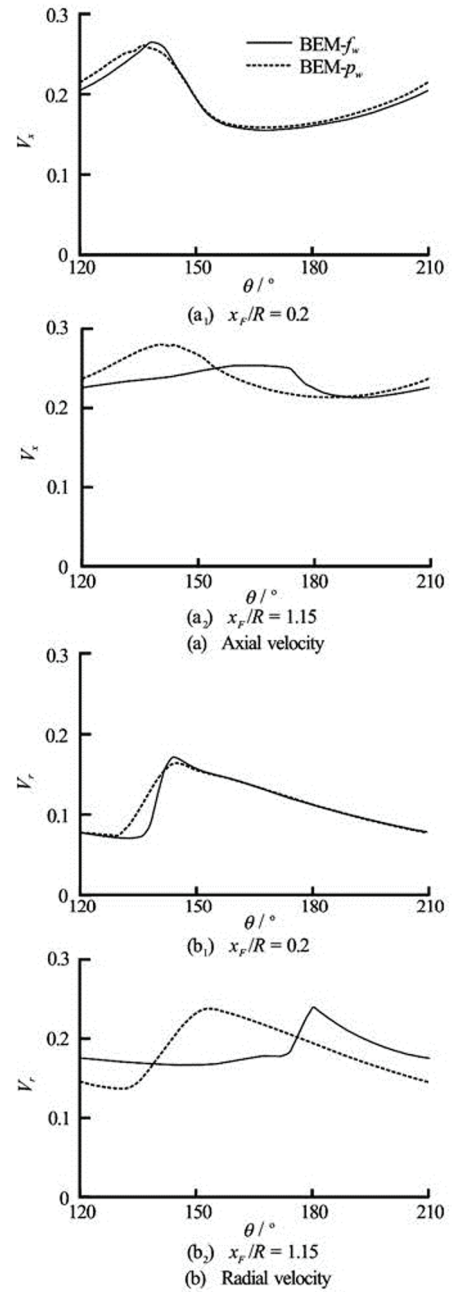


Fig.8 Perturbation velocity for  $J = 0.88$  on planes at  $x_F/R = 0.2$  and  $x_F/R = 1.15$ , radial position  $r/R = 0.7$ . BEM prescribed ( $p_w$ ) and free-wake ( $f_w$ ) results are compared

velocity field, as shown in Fig.8 where axial (top) and

radial (bottom) velocity components, along a circle of radius  $r/R = 0.7$  on the above transversal planes, are plotted. Velocity distributions at  $x_F/R = 0.2$  are comparable, whereas moving further downstream the two wake models yield completely different results. Recalling propeller loads predictions in Fig.4, it may be noted that  $K_T$  and  $K_Q$  values predicted by the two alternative wake models show negligible differences at  $J = 0.88$ . This is not surprising because blade loading is relatively low ( $K_T = 0.157$ ), shed vortices have a limited strength and hence only the wake portion close to the propeller affects the hydrodynamic loads. These findings confirm that a rigid wake modelling (even if tailored to the particular case), suited for the analysis of propeller performance, may be not adequate to capture the vortex-sheet shape and, in turn, the downstream flow-field velocities. For a reliable prediction of these characteristics the use of a free-wake model is mandatory, in particular for lower values of the advance coefficient.

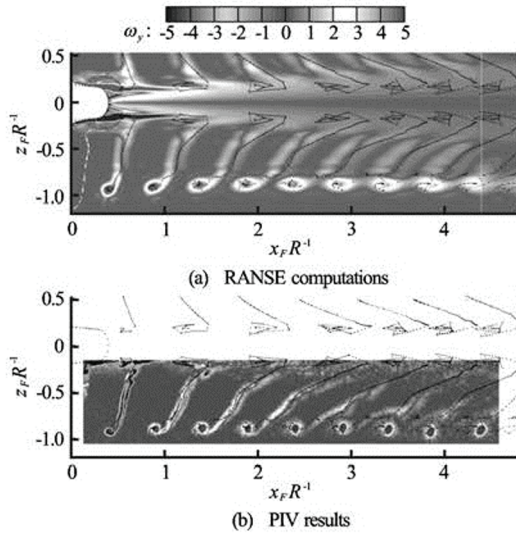


Fig.9 Vorticity distribution downstream the propeller on  $y_F/R = 0$  plane for  $J = 0.88$ . PIV results (bottom) compared to RANSE computations (top) and trailing wake surface position predicted by BEM (black lines)

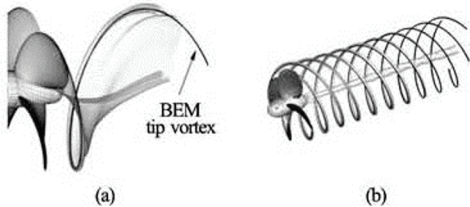


Fig.10 Tip-vortex location by BEM (left), tip-vortices location predictions by BEM (black lines) and RANSE for  $J = 0.88$  (right)

In order to address an in-depth analysis, free-

wake BEM results are hereafter compared with RANSE computations and experimental data obtained through the PIV technique<sup>[26]</sup>. Figure 9 shows the contour levels of the transversal component ( $\omega_y$ ) of the vorticity field calculated by RANSE (top) and measured by PIV (bottom) on the longitudinal plane  $y_F/R = 0$ . BEM trailing wake location, shown by black lines, is superposed to both data sets. Main flow features described by PIV are well captured by RANSE, especially in terms of tip-vortices intensity and spacing. However, the smearing of blades trailing wake indicates excessive eddy viscosity. Other discrepancies also appear in the evaluation of the wake pitch at inner radii, that seems to be slightly underestimated with respect to experiments; this fact is directly correlated with the slight underprediction of  $K_T$  (recall

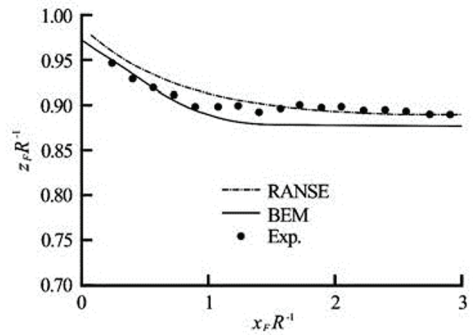


Fig.11 Prediction of tip-vortices location on plane  $y_F/R = 0$  for  $J = 0.88$

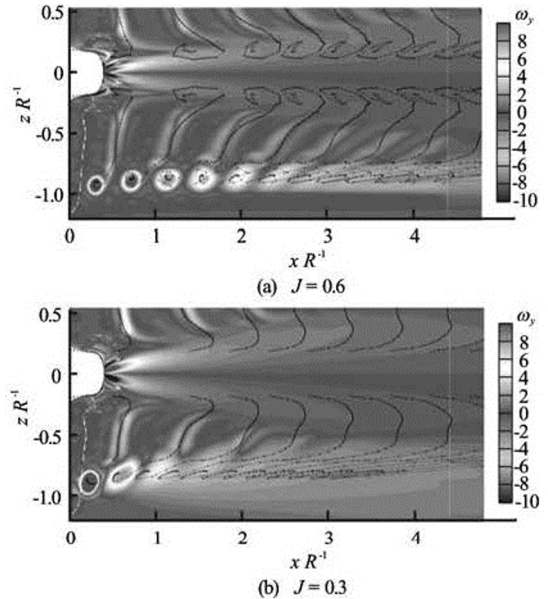


Fig.12 Vorticity distribution downstream the propeller at  $y_F/R = 0$  plane for  $J = 0.6$  (top) and  $J = 0.3$  (bottom). RANSE results are compared to trailing wake surface position predicted by BEM (black lines)

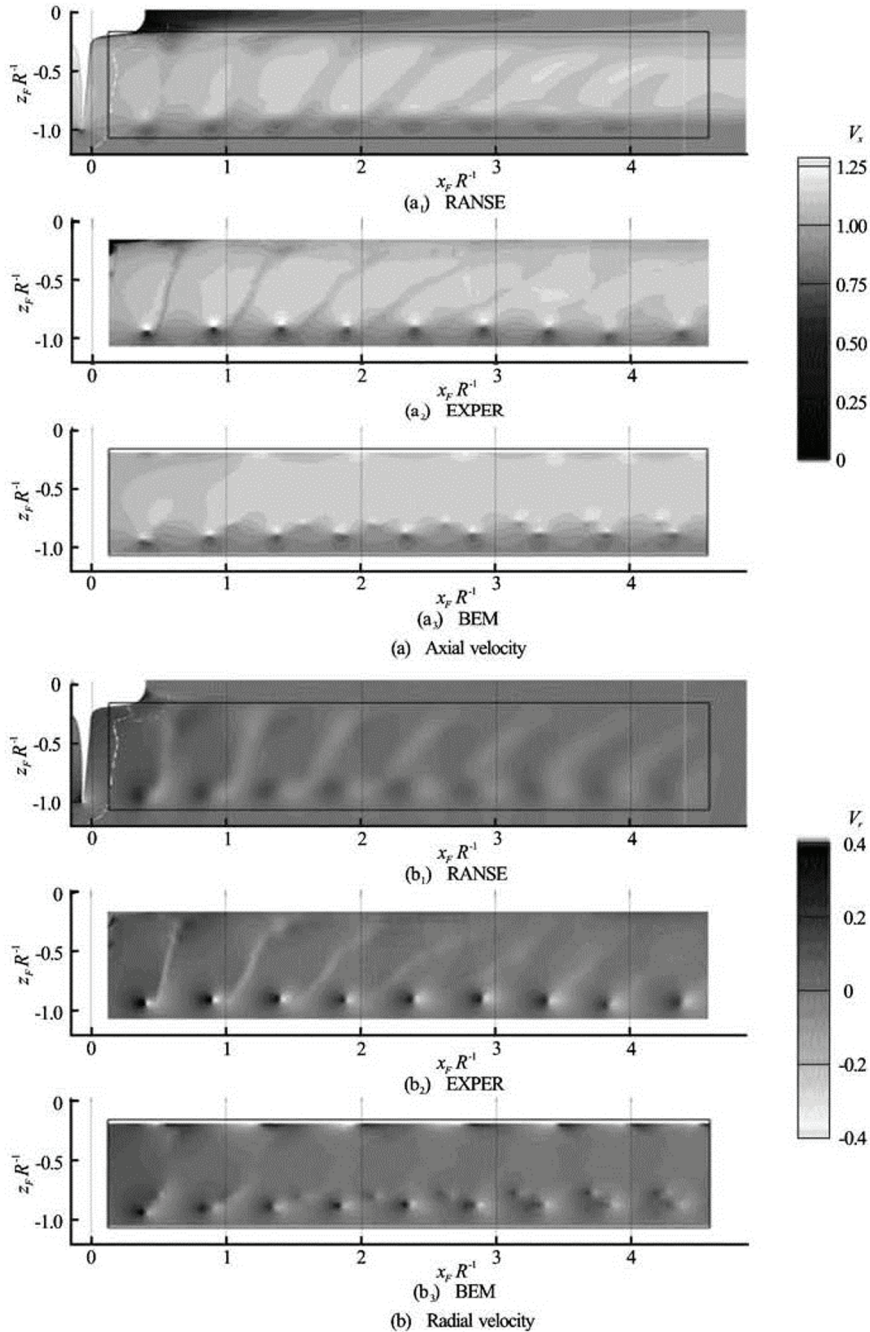


Fig.13 Total velocity distribution downstream the propeller, on  $y_F / R = 0$  plane ( $J = 0.88$ ). BEM, RANSE and PIV data are compared. The rectangular box superimposed to RANSE contour plots identifies BEM and experimental measurement windows. From top to bottom: axial and radial velocity

Fig.6). In terms of potential flows, BEM predictions of blade trailing-wake locations are in good agreement with both experiments and RANSE simulations up to  $x_F / R = 4.5$ , where tip-vortex/trailed-wake interaction is well solved. Furthermore, the growth of the tip-vortex size moving downstream is well predicted respect to RANSE outcomes; this is particularly true for  $x_F / R < 3.0$ , whereas, further downstream, the tip-vortex/trailed-wake interaction tends to render the wake alignment procedure unstable, albeit the general shape of

the trailed-wake is yet satisfactorily described. Note that BEM flow solution in the region close to the rotation axis is dominated by the presence of rolled-up vortices, similarly to what happens at the blade tip; such an unphysical solution is mainly due to the lack of a suitable doublets sheet model convected downstream the hub, interacting with blades vorticity. In that flow region, experimental data are not available because of the lack of optical access, correctly, RANSE calculations show the presence of a hub-vortex close

to the propeller disk. The general quality of BEM predictions may be appreciated in terms of blade tip-vortex location, herein defined as the trajectory of the centre of figure of the panels centroids localized in the outer portion of the blade ( $r/R > 0.9$ , see Fig.10 (left)). To this aim, in Figs.10 (right) and Fig.11, BEM tip-vortex position is compared with the vortical structures identified in both RANSE and experimental data. In details, in Fig.10 (right) tip-vortex trajectory by BEM is compared (up to  $x_F/R = 5.0$ ) with the iso-surface of the 2<sup>nd</sup> eigenvalue of tensor ( $\mathcal{S}^2 + \boldsymbol{\Omega}^2$ ), that, as proposed by Jeong and Hussain<sup>[28]</sup>, provides a consistent marker of vortical coherent structures ( $\mathcal{S}$  and  $\boldsymbol{\Omega}$  denote the symmetric/emisymmetric components of the rate of strain tensor, respectively), as shown, the agreement is very good as far as RANSE simulation can identify the vortex. Differently, Fig.11 compares the tip-vortex position on the  $y_F/R = 0$  plane predicted by BEM with those given by RANSE and with PIV data. The level of accuracy of BEM outcomes is similar to RANSE results, in that wake contraction is well predicted by both solvers, with comparable numerical/experimental discrepancies.

Flow-field features at different operating conditions, namely  $J = 0.6$  and  $J = 0.3$ , are shown in Fig.12 where RANSE and BEM results are compared, as expected, the higher blade loading induces a smaller wake pitch and a greater strength of tip-vortices. Time-resolved visualizations of the propeller wake<sup>[29]</sup> highlight that, in these working conditions (especially at  $J = 0.3$ ), the wake structure is dominated by spatial and temporal instabilities. In these conditions, it is well known that RANSE modelling is inadequate to capture wake evolution and stability, thus approaches like large eddy simulations (LES) or detached eddy simulations (DES) become mandatory<sup>[15]</sup>. In fact, RANSE simulations capture tip-vortex structures close to the propeller plane and identify a region of diffused vorticity downstream, axially longer for lower values of  $J$ . Despite this complex wake structure, BEM hydrodynamics is yet able to track tip-vortices and predict wake contraction, as long as the wake does not coalesce into diffused vorticity.

Next, an investigation in terms of total velocity field downstream the propeller disk is performed. Figure 13 depicts a numerical/experimental comparison in terms of axial and radial velocity components for the design condition. As previously discussed for the vorticity field, BEM yields a good agreement with RANSE and PIV results. In detail, BEM capability in capturing velocity peaks near tip-vortices and describing flow regions not dominated by viscosity driven phenomena (which are smeared by RANSE computa-

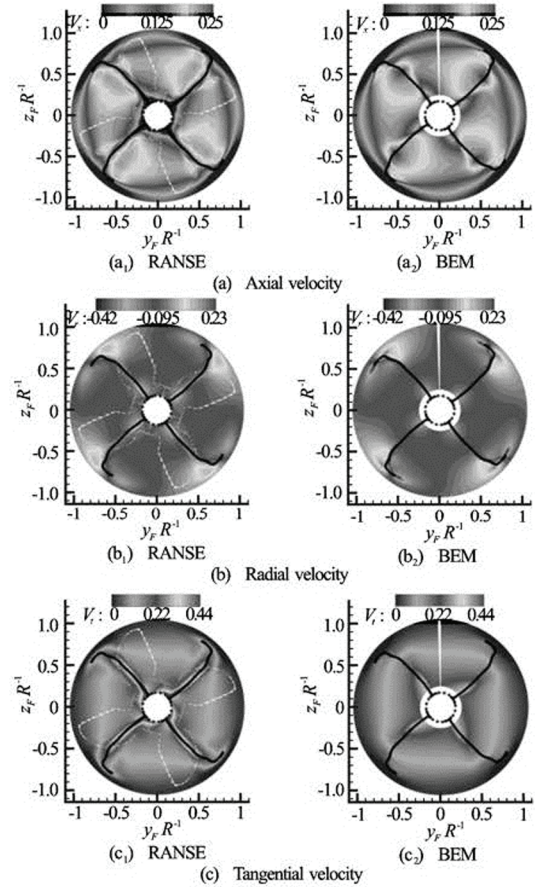


Fig.14 BEM and RANSE perturbation velocity distribution downstream the propeller on  $x_F/R = 0.2$  plane ( $J = 0.88$ ). From top to bottom: axial, radial and tangential velocity

tions) is highlighted. Moreover, the flow analysis on transversal planes normal to the propeller axis is shown by Fig.14 where axial, radial and tangential perturbation velocities at  $x_F/R = 0.2$  are depicted. Here, RANSE computations (left) and BEM predictions (right) are compared. In both figures, the position of the potential trailing wake, shown by black lines, almost perfectly matches the trace of the viscous wake. As a general statement, BEM outcomes are in good agreement with RANSE results, even though velocity peaks are a bit higher. The analysis of the radial velocity field (see Fig.14, centre) highlights the capability of the BEM-based approach to correctly describe strong flow acceleration or deceleration near blade tip-vortices and slipstream contraction. Similarly, the analysis of the tangential velocity (Fig.14, bottom) shows that slipstream rotation induced by the propeller is well captured by BEM, outside the viscous wake regions. Moving further downstream, at  $x_F/R = 1.15$ , Fig.15 shows the same type of comparison. The good quality of BEM results is confirmed.

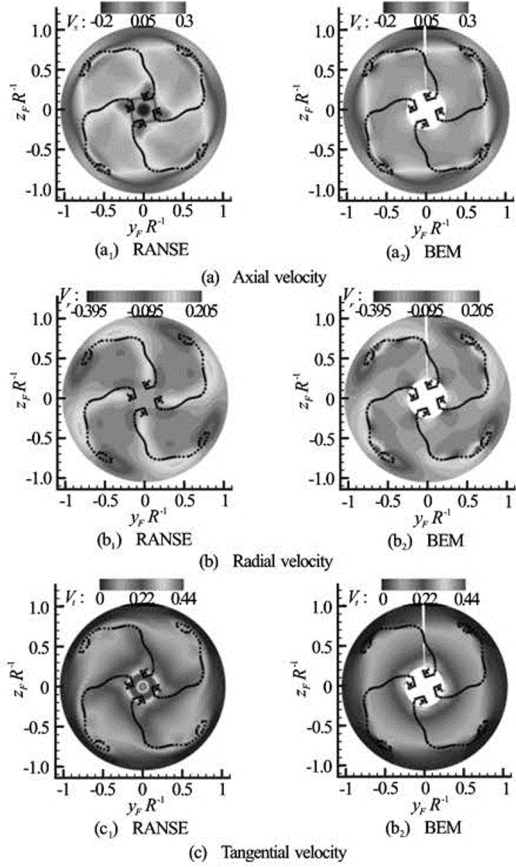


Fig.15 BEM and RANSE perturbation velocity distribution downstream the propeller on  $x_F / R = 1.15$  plane ( $J = 0.88$ ). From top to bottom: axial, radial and tangential velocity

A local comparison in terms of velocity fields is provided in Fig.16, showing axial (left) and radial (right) velocity components at circles identified by  $r / R = 0.3, 0.5, 0.7$  and  $0.9$  (from top to bottom) on the plane at  $x_F / R = 0.2$ . For each radial section, a quarter of revolution is depicted. From a general standpoint the velocity components by BEM are in satisfactory agreement with both experiments and RANSE simulations throughout the considered domain, except for the azimuthal region dominated by the viscous wake (approximately located at  $\theta \cong 140^\circ$ ). Recalling that the azimuthal location of the potential wake well matches the viscous wake (see Figs.14 and 15), differences between BEM and reference data in this narrow region can be motivated by the finite vortex core model introduced to describe the induced flow-field. As expected, RANSE computations yield a fair agreement with PIV measurements including the viscous wake region. Moving downstream, Fig.17 shows the same analysis on the plane at  $x_F / R = 1.15$ . Here, the quality of BEM

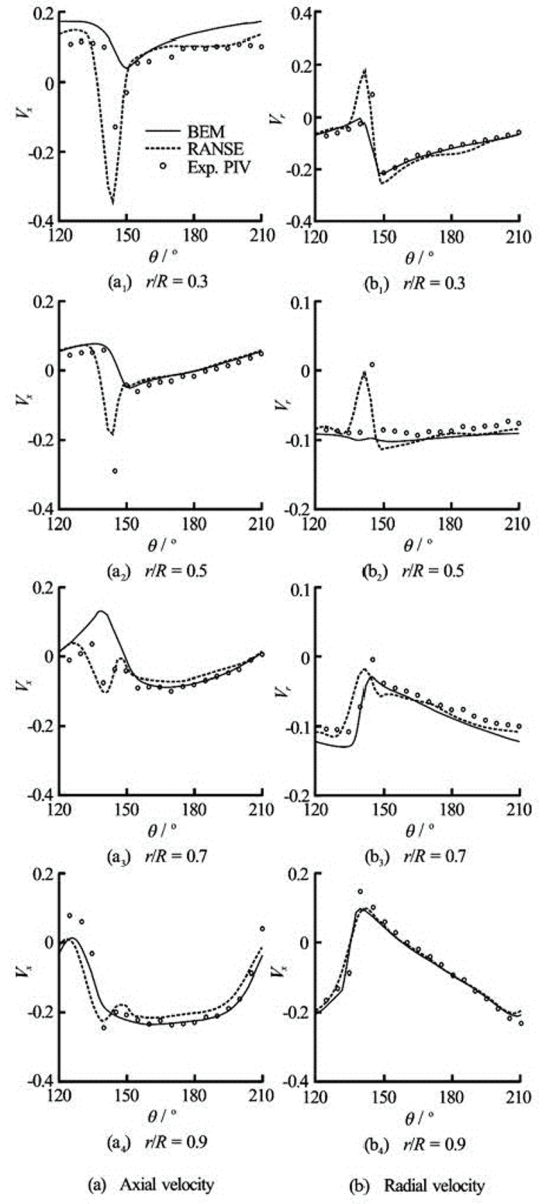


Fig.16 Perturbation velocity for  $J = 0.88$  on a transversal plane at  $x_F / R = 0.2$  and radial positions (from top to bottom)  $r / R = 0.3, 0.5, 0.7, 0.9$ . BEM and RANSE results are compared to PIV data. Axial velocity (left) and radial velocity (right)

outcomes is still satisfactory, whereas a general worsening of the agreement between RANSE computations and experiments arises because of incorrect eddy viscosity values. Heavier loading conditions at  $J = 0.6$  are depicted in Fig.18 that refers to velocity fields on orthogonal planes placed at  $x_F / R = 0.2$  and  $1.15$ . For this condition PIV experiments are not available, thus only BEM and RANSE predictions at  $r / R = 0.5$  and  $0.9$  are compared. In all cases, the azimuthal position of the wake is well captured by the BEM app-

roach, as already observed in the analysis of the vorticity field; the agreement in terms of magnitude is generally reasonable, although discrepancies increase on the farthest plane.

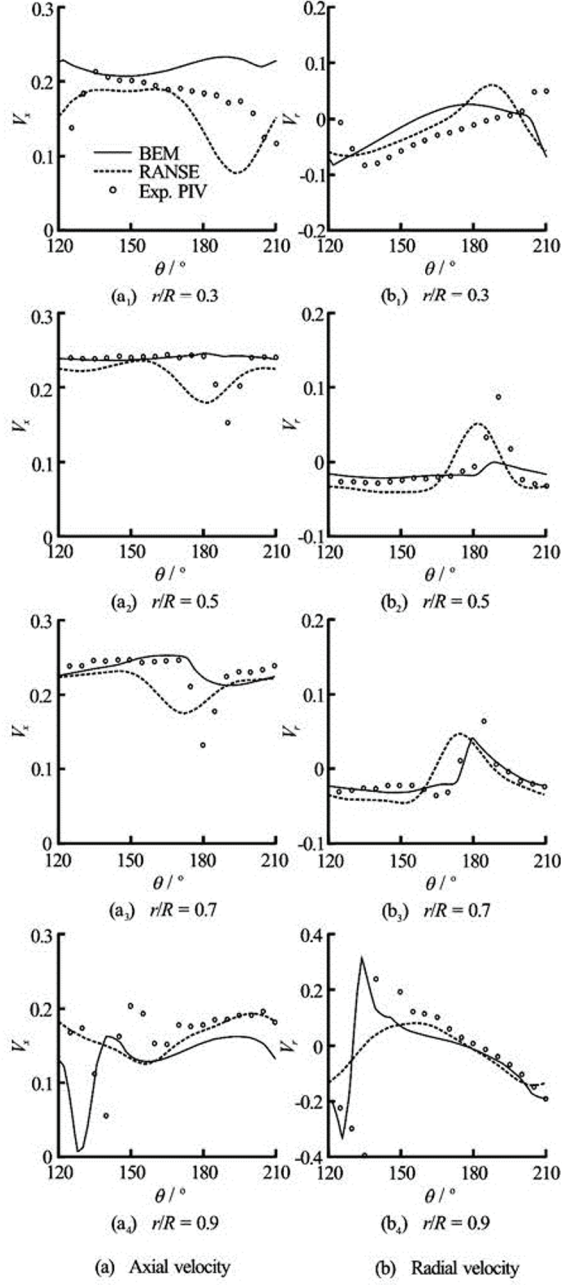


Fig.17 Perturbation velocity for  $J = 0.88$  on a transversal plane at  $x_F/R = 1.15$  and radial positions (from top to bottom)  $r/R = 0.3, 0.5, 0.7, 0.9$ . BEM and RANSE results are compared to PIV data. Axial velocity (left) and radial velocity (right)

In conclusion, the above analysis demonstrates the high quality of free-wake BEM predictions in terms of wake pitch and tip roll-up at the design conditions, yielding, in turn, reliable velocity field distributions downstream. The level of accuracy decreases

beneath the design condition although it remains satisfactory closer to the propeller disk.

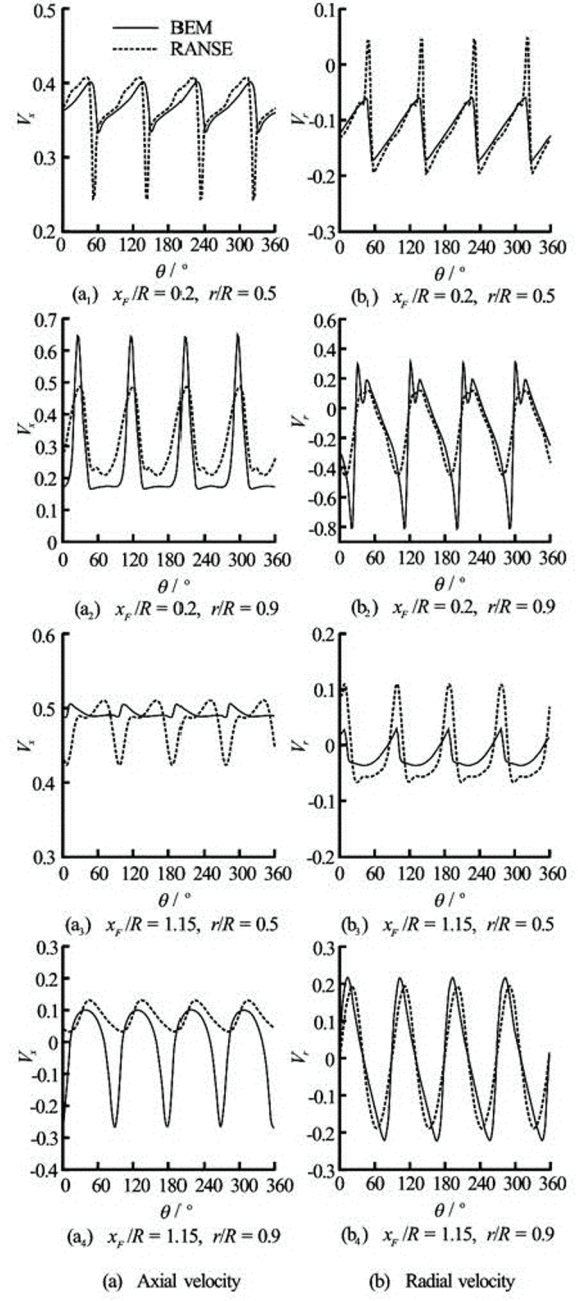


Fig.18 Perturbation velocity for  $J = 0.6$ : BEM and RANSE results compared. Axial velocity (left) and radial velocity (right). From top to bottom:  $[x_F/R = 0.2, r/R = 0.5]$ ,  $[x_F/R = 0.2, r/R = 0.9]$ ,  $[x_F/R = 1.15, r/R = 0.5]$  and  $[x_F/R = 1.15, r/R = 0.9]$

### 2.3 Blade pressure distribution

Blade pressure distribution obtained by BEM is here compared to that predicted by RANSE. No experimental data are available. Chordwise amplitude of the nondimensional pressure coefficient  $c_p = 2(p -$

$p_0)/\rho n^2 D^2$  is depicted on blade sections located at  $r/R = 0.33, 0.5, 0.725, 0.83, 0.91, 0.94$  at different working points, namely  $J = 0.3, 0.6$  and  $0.88$ . BEM results are obtained by using both the free-wake algorithm ( $f_w$ ) and the *ad-hoc* prescribed wake modelling ( $p_w$ ). Figure 19 refers to  $J = 0.88$ . As shown, at the design condition the BEM/RANSE agreement is excellent for both wake models, worse agreement is observed for the inner section loads which, however, are significantly lower in terms of peak-to-peak variations. Hence, similarly to the analysis of prope-

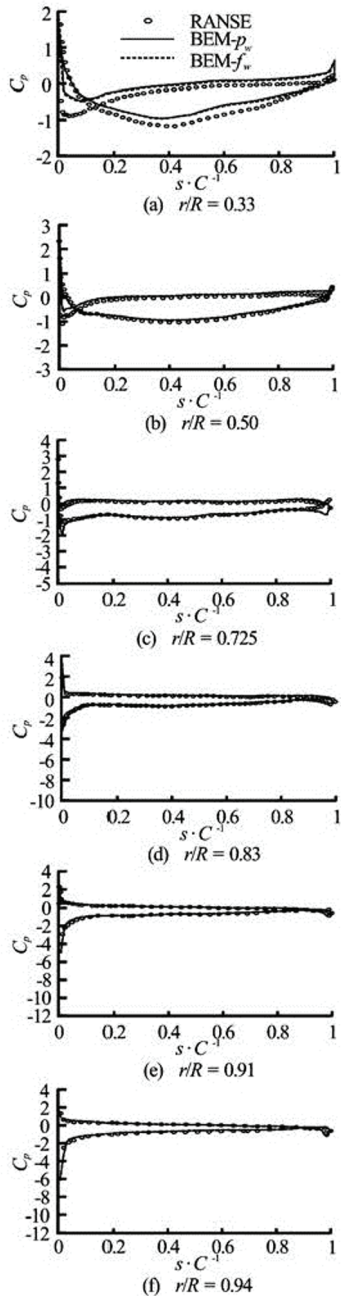


Fig.19 Blade pressure by BEM and RANSE,  $J = 0.88$

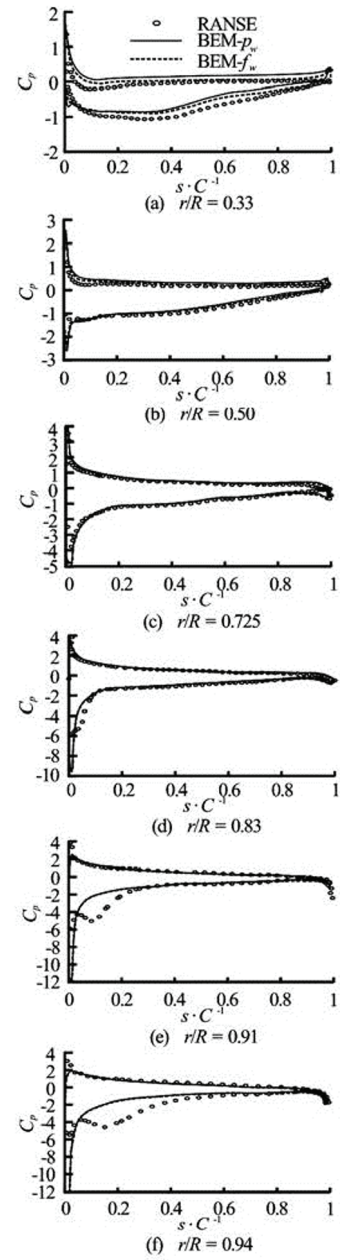


Fig.20 Blade pressure by BEM and RANSE,  $J = 0.6$

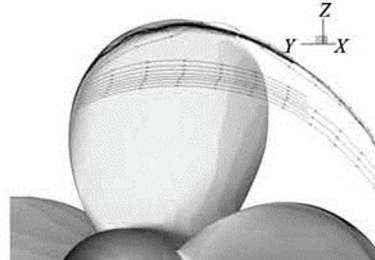


Fig.21 Leading edge vortex at the blade suction side by streamlines visualization. RANSE computations for  $J = 0.6$

ller thrust/torque, the *ad-hoc* prescribed wake

modelling confirms to be fully adequate to capture the pressure distribution upon blades. At  $J = 0.6$  (Fig.20) the BEM/RANSE comparison is still very good at the inner and mid sections. However, respect to the design condition, a first forking between  $f_w$  and  $p_w$  results appears near the root of the blade, where the  $f_w$  exhibits a slightly better agreement with RANSE data. On the contrary, at the outer sections ( $r/R = 0.91$  and  $r/R = 0.94$ ), the pressure distribution near the leading edge on the suction side of the blade diverges from the trend predicted by RANSE. This is caused by the for-

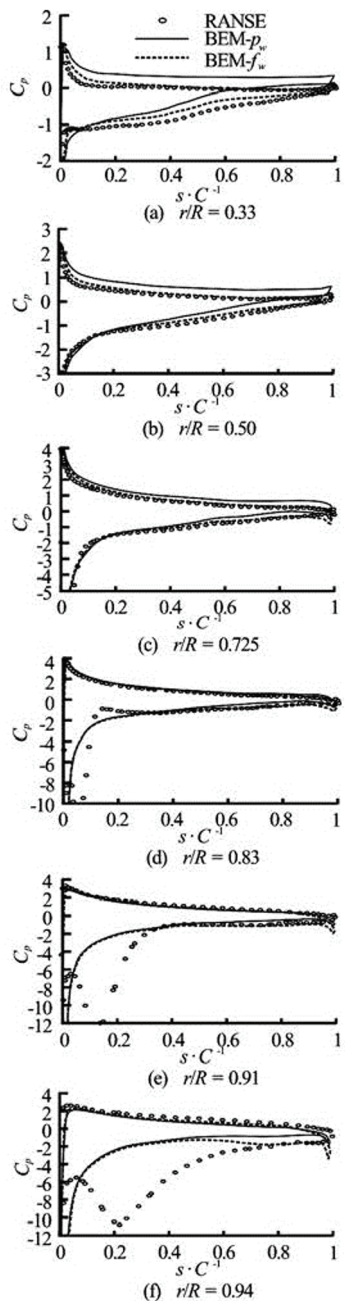


Fig.22 Blade pressure by BEM and RANSE,  $J = 0.3$

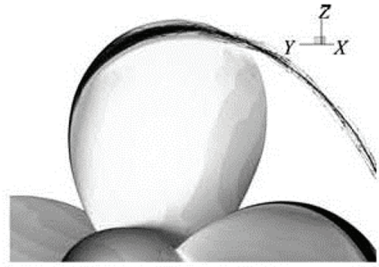


Fig.23 Leading edge vortex at the blade suction side by streamlines visualization. RANSE computations for  $J = 0.3$

mation of a leading-edge vortex, clearly shown in Fig.21 through the visualization of volume streamlines computed by RANSE, which is not modelled by the BEM approach. At higher loading conditions ( $J = 0.3$ , Fig.22) both magnitude and size of the leading-edge vortex increase, (see Fig.23), thus inducing significant lower pressure peaks on the suction side of the outer blade sections not captured by the BEM solver. Note that the lower advance coefficient determines a wake-sheet closer to the propeller disk, therefore, differently from the previous cases, the use of the free-wake modelling is needed to enhance BEM results.

#### 2.4 Propeller noise signature

In this section, BEM-RANSE pressure disturbance signatures at virtual hydrophones located downstream the propeller disk are compared. The free-wake panel method is used firstly to detect the hydrodynamic sources of sound and then the Bernoulli equation is used as hydroacoustic solver to radiate the hydrodynamic “noise” in the flow-field. It is worthy note that neither BEM nor RANSE solvers include compressibility effects, thus, pressure disturbance signatures should be referred to as *pseudo-noise* signals<sup>[10]</sup>. For this reason, the comparison is here intended only for cross-validation purposes between two different approaches. Figure 24 shows the BEM/RANSE comparison in terms of (pseudo-) noise evaluated at three virtual hydrophones located in the  $y_F/R = 0$  plane, at a distance  $x_F/R$  from the rotor hub of 0.2 and 1.15, respectively. Hydrophones are placed outside the wake streamtube, at a vertical distance  $z_F/R$  equal to 1.0, 1.1, and 1.3, respectively. As highlighted, there is a very good agreement for each set of hydrophones, both in terms of phase signals and magnitude. Akin to the analysis of the velocity field discussed in Fig. 17, a slightly lower level of agreement is exhibited for points located at  $x_F/R = 1.15$ , albeit the general agreement between signals remains acceptable.

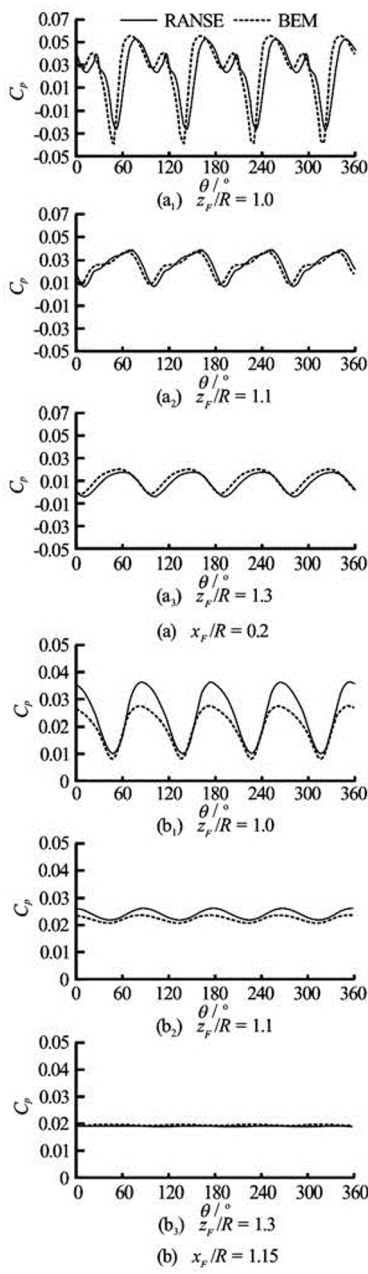


Fig.24 Time history of pressure disturbance in the flow-field for  $J = 0.88$ . BEM and RANSE predictions compared at  $x_F/R = 0.2$  (left) and  $x_F/R = 1.15$  (right) planes. From top to bottom: hydrophones at  $z_F/R = 1.0, 1.1$  and  $1.3$

### 3. Conclusions

In this paper, drawbacks and capabilities of a Boundary Element Method for the analysis of marine propeller hydrodynamics in uniform onset flow are investigated through comparison with experimental data and RANSE simulations. The proposed panel method is combined both with a non-linear alignment technique to describe the free-wake shape, and an Iterative Pressure Kutta (IPK) condition to assure no

finite pressure jump at blades trailing edges. A comprehensive investigation on propeller loads, slipstream velocities, wake shape, blade pressure distribution and pressure disturbance in the flow-field is presented. The validation study is performed by considering a four-bladed model propeller. Numerical results confirm the capability of free-wake/BEM-IPK hydrodynamics in capturing propeller thrust and torque over a wide range of operating conditions.

Correlation of open water loads predictions with analysis of induced velocity and vorticity fields, demonstrates how a simplified prescribed wake model is generally sufficient to describe thrust, torque, blade pressure distributions and pseudo-noise signals when propeller is moderately loaded or unloaded, whereas a free-wake modeling is necessary to well capture the wake pitch that strongly affects propeller performance at high loading conditions. Note that other effects related to roll-up and wake contraction are of minor relevance. Differently, a correct evaluation of slipstream velocity and vorticity distribution requires the wake alignment at any loading conditions. As a matter of fact, the trailing wake surface determined by BEM is accurate in terms of pitch distribution, slipstream contraction and tip-vortices location; this is especially true close to the design advance ratio, where the agreement with RANSE computations and experimental data is very good, as long as diffusive or dissipative driven effects make the comparison meaningful. Beneath the design working point, an overall worsening of BEM results is observed; this fact is not surprising since the more complex shape of the rolled-up wake makes the wake alignment procedure prone to numerical instabilities during the convergence solution seeking. Furthermore, the inception of a leading-edge tip vortex (not modeled by the present BEM formulation) and the excessive eddy viscosity associated to RANSE computations contribute to the lower level of agreement with both RANSE and experiments (if available). In conclusion, the quality of the numerical results make the proposed 3-D free-wake BEM hydrodynamic approach suited for the analysis of marine propellers; in particular the capability to capture a reasonable wake structure makes the algorithm appealing for the study of configurations with significant wake-body interactions.

### Acknowledgement

The authors wish to thank Dr. Francesco Salvatore for his valuable contribution in the development of the BEM hydrodynamic solver.

### References

- [1] KERWIN J. E., LEE C. S. Prediction of steady and unsteady marine propeller performance by numerical lif-

- ting-surface theory[J]. **Society of Naval Architects and Marine Engineers-Transactions**, 1978, 86: 1-30.
- [2] HOSHINO T. Hydrodynamic analysis of propellers in steady flow using a surface panel method, 2nd report: Flow field around propeller[J]. **Journal of the Society of Naval Architects of Japan**, 1989, 166: 79-92.
- [3] GREELEY D. S., KERWIN J. E. Numerical methods for propeller design and analysis in steady flow[J]. **Society of Naval Architects and Marine Engineers-Transactions**, 1982, 90: 416-453.
- [4] KINNAS S. A., PYO S. Cavitating propeller analysis including the effects of wake alignment[J]. **Journal of Ship Research**, 1999, 43(1): 38-47.
- [5] LIU P., COLBOURNE B. A study of wake discretization in relation to the performance of a propeller panel method[J]. **Ocean Engineering International**, 2002, 6(1): 32-39.
- [6] POLITIS G. K. Unsteady rollup modeling for wake-adapted propellers using a time-stepping method[J]. **Journal of Ship Research**, 2005, 49(3): 216-231.
- [7] TIAN Y., KINNAS S. A. A wake model for the prediction of propeller performance at low advance ratios[J]. **International Journal of Rotating Machinery**, 2012, 2012: doi: 10.1155/2012/372364.
- [8] KINNAS S. A., TIAN Y. and SHARMA A. Numerical modeling of a marine propeller undergoing surge and heave motion[J]. **International Journal of Rotating Machinery**, 2012, 2012: doi: 10.1155/2012/257461.
- [9] DURANTE D., DUBBIOSO G. and TESTA C. Simplified hydrodynamic models for the analysis of marine propellers in a wake-field[J]. **Journal of Hydrodynamics**, 2013, 25(6): 954-965.
- [10] TESTA C., IANNIELLO S. and SALVATORE F. et al. Numerical approaches for hydroacoustic analysis of marine propellers[J]. **Journal of Ship Research**, 2008, 52(1): 57-70.
- [11] GENNARETTI M., TESTA C. and BERNARDINI G. An unsteady aerodynamic formulation for efficient rotor tonal noise prediction[J]. **Journal of Sound and Vibration**, 2013, 332(25): 6743-6754.
- [12] SALVATORE F., TESTA C. and GRECO L. A viscous/inviscid coupled formulation for unsteady sheet cavitation modelling of marine propellers[C]. **CAV 2003 Symposium**. Osaka, Japan, 2003.
- [13] SALVATORE F., TESTA C. and GRECO L. Coupled hydrodynamics-hydroacoustics BEM modelling of marine propellers operating in a wakefield[C]. **1st International Symposium on Marine Propulsion (SMP 2009)**. Trondheim, Norway, 2009.
- [14] MUSCARI R., FELLI M. and DI MASCIO A. Analysis of the flow past a fully appended hull with propellers by computational and experimental fluid dynamics[J]. **Journal of Fluids Engineering**, 2011, 133(6): 061104.
- [15] MUSCARI R., DI MASCIO A. and VERZICCO R. Modeling of vortex dynamics in the wake of a marine propeller[J]. **Computers and Fluids**, 2013, 73: 65-79.
- [16] GRECO L., SALVATORE F. and DI FELICE F. Validation of a quasi-potential flow model for the analysis of marine propellers wake[C]. **25th ONR Symposium on Naval Hydrodynamics**. St. John's, Canada, 2004.
- [17] MORINO L. Boundary integral equations in aerodynamics[J]. **Applied Mechanics Reviews**, 1993, 46(8): 445-466.
- [18] CARLTON J. S. **Marine propellers and propulsion**[M]. Third Edition, Oxford, UK: Butterworth-Heinemann, 2012.
- [19] GRIGSON C. W. B. A planar friction algorithm and its use in analysing hull resistance[J]. **Transactions of the Royal Institution of Naval Architects**, 2000, 142: 76-115.
- [20] LEONE S., TESTA C. and GRECO L. et al. Computational analysis of self-pitching propellers performance in open water[J]. **Ocean Engineering**, 2013, 64: 122-134.
- [21] SUCIU E., MORINO L. Non linear steady incompressible lifting-surface analysis with wake roll-up[J]. **AIAA Journal**, 1977, 15(1): 54-58.
- [22] DI MASCIO A., BROGLIA R. and MUSCARI R. Prediction of hydrodynamic coefficients of ship hulls by high-order Godunov-type methods[J]. **Journal of Marine Science and Technology**, 2009, 14(1): 19-29.
- [23] MERKLE C. L., ATHAVALE M. Time-accurate unsteady incompressible flow algorithm based on artificial compressibility[R]. AIAA Paper 87-1137, 1987.
- [24] BEAM R. M., WARMING R. F. An implicit factored scheme for the compressible Navier-Stokes equations[J]. **AIAA Journal**, 1978, 16(4): 393-402.
- [25] FAVINI B., BROGLIA R. and DI MASCIO A. Multigrid acceleration of second order ENO schemes from low subsonic to high supersonic flows[J]. **International Journal of Numerical Method Fluids**, 1996, 23(6): 589-606.
- [26] DI FELICE F., DI FLORIO D. and FELLI M. et al. Experimental investigation of the propeller wake at different loading conditions by particle image velocimetry[J]. **Journal of Ship Research**, 2004, 48(2): 168-190.
- [27] ROACHE P. J. Quantification of uncertainty in computational fluid dynamics[J]. **Annual Review Fluid Mechanics**, 1997, 29: 123-160.
- [28] JEONG J., HUSSAIN F. On the identification of a vortex[J]. **Journal of Fluid Mechanics**, 1995, 285: 69-94.
- [29] FELLI M., CAMUSSI R. and DI FELICE F. Mechanisms of evolution of the propeller wake in the transition and far fields[J]. **Journal of Fluid Mechanics**, 2011, 682: 5-53.
- [30] KERWIN J. E., KINNAS S. A. and LEE J.-T. et al. A surface panel method for the hydrodynamic analysis of ducted propellers[J]. **Society of Naval Architects and Marine Engineers-Transactions**, 1987, 95: 93-122.

## Appendix A

Let us consider a Z-bladed propeller working in open water conditions. Two frames of reference, depicted in Fig.1, are introduced: the rotating frame of reference (RFR) ( $O, x, y, z$ ) fixed with the reference blade and the fixed frame of reference (FFR) ( $O, x_F, y_F, z_F$ ) rigidly connected to the propeller shaft housing. By enforcing the integral solution of the Laplace equation on the propeller surface, the application of a zero-th order BEM yields

$$\frac{1}{2} \varphi_{ij} = \sum_{n=1}^{N_B+N_H} \sum_{m=1}^{M_B+M_H} (S_{ij,mn} \chi_{mn} + D_{ij,mn} \varphi_{mn}) + \sum_{n=1}^{N_W} \sum_{m=1}^{M_W} D_{ij,mn} \Delta \varphi_{mn} \quad (A1)$$

where  $\varphi$ ,  $\partial\varphi/\partial n$ , and  $\Delta\varphi$  are assumed piecewise constant on each  $lk$  panel ( $x_{lk}$  indicates the collocation point),  $M_B$  and  $N_B$  the number of chordwise and spanwise blade panels,  $M_w$  and  $N_w = N_B$  the number of streamwise and radial wake panels, whereas  $M_H$  and  $N_H$  represent the number of circumferential and axial hub panels, respectively. In addition,  $\Delta\varphi_{mn} = \Delta\varphi(x_{mn})$ , whereas  $\chi_{mn} = (\partial\varphi/\partial n)_{mn}$  stems from the impermeability condition  $(v_i + \nabla\varphi) \cdot \mathbf{n} = 0$ . Equation (A1) holds for a single-bladed propeller, the extension to the  $Z$ -bladed case is straightforward. For clarity, Fig.1A shows the topology concerning with the computational grid used on a single blade and on a hub sector. The time-independent coefficients appearing in Eq.(A1) are given by

$$\begin{aligned} S_{ij,mn} &= - \int_{S_{mn}} \frac{1}{4\pi \|x_{ij} - \mathbf{y}\|} dS(\mathbf{y}), \\ D_{ij,mn} &= \int_{S_{mn}} \frac{\partial}{\partial n} \frac{1}{4\pi \|x_{ij} - \mathbf{y}\|} dS(\mathbf{y}) \end{aligned} \quad (A2)$$

where  $S_{mn}$  is the body or wake panel surface. To solve Eq.(A1) the evolution equation for  $\Delta\varphi$  is combined with the Kutta-Morino hypothesis<sup>[17]</sup>, yielding

$$\begin{aligned} \Delta\varphi_{mn}(t) &= \varphi_{1n}(t - \tau_{mn}) - \varphi_{M_B n}(t - \tau_{mn}), \\ n &= 1, N_w, \quad m = 1, M_w \end{aligned} \quad (A3)$$

with  $\tau_{mn}$  denoting the time-delay required for a material wake grid point to be convected from the  $mn$  trailing-edge panel to  $x_w$ . Equations (A1) and (A3) provide the velocity potential field upon  $S_B$ ; then, the application of the Bernoulli equation (see Eq.(2)) yields the pressure distribution upon the blades. However, for blade shapes with blunt trailing-edges, the Kutta-Morino condition fails and, in turn, Eq.(A3) is no longer valid. In these cases, the assumption of no vortex filament at the blade trailing-edge is assured by imposing directly a zero pressure jump

$$\Delta p_n = p_{1n} - p_{M_B n} = 0, \quad n = 1, N_B \quad (A4)$$

Due to the nonlinear relationship between  $\Delta p$  and  $\varphi$ , an iterative method is needed to solve Eqs.(A1) and (A4) jointly. By defining  $\Delta\varphi^T = (\Delta\varphi_1^{TE}, \dots, \Delta\varphi_{N_B}^{TE})$  and  $\Delta p^T = (\Delta p_1, \dots, \Delta p_{N_B})$ , the Newton-Raphson scheme at the  $k$ -th iteration step, provides

$$\Delta\varphi^{(k+1)} \cong \Delta\varphi^{(k)} - \mathbf{J}^{(k)-1} \Delta p^{(k)} \quad (A5)$$

where  $\mathbf{J}$  denotes the Jacobian matrix of the problem. To reduce the computational costs, the Jacobian matrix is kept constant during the iteration procedure, thus

$$J_{ij}^{(k)} = J_{ij} \cong \frac{\Delta p_i^{(\beta)} - \Delta p_i^{(0)}}{\Delta\varphi_j^{TE(\beta)} - \Delta\varphi_j^{TE(0)}} \quad (A6)$$

where superscript 0 corresponds to the solution coming from the use of Kutta-Morino condition whereas superscript  $\beta$  refers to the solution obtained by perturbing  $\Delta\varphi_j^{TE}$  to comply with  $\Delta\varphi_j^{TE(\beta)} = (1 + \beta)\Delta\varphi_j^{TE(0)}$ . The parameter  $\beta$  is  $\ll 1$ , throughout the paper,  $\beta = 0.01$  is used. Once the Jacobian matrix is known, Eq.(A5) is used iteratively as long as convergence is reached. The combined solution of Eqs.(A1) and (A5) defines the Iterative Pressure Kutta (IPK) algorithm<sup>[30]</sup>. It is worth noting that the use of the IPK solver in presence of the free-wake analysis is obtained following a two steps procedure where, firstly, the converged wake is computed and then is used as it were a prescribed wake into the IPK method.

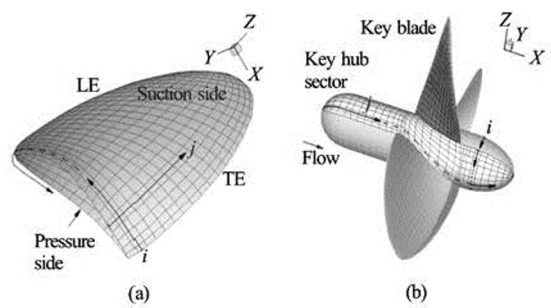


Fig.1 A Blade (left) and propeller (right) computational grids for BEM calculations: definition of indices convention